Correspondence to:

C. Rino,
crino@comcast.net

On Phase Screen Models for Scintillation Diagnostics

Charles Rino[1] , Charles Carrano[1] , Dmytro Vasylyev[2] , Theodore Beach[1], Brian Breitsch[3], Yu Morton[3], and Keith Groves[1]

[1]Institute for Scientific Research, Boston College, Newton, MA, USA, [2]Solar-Terrestrial Physics, German Aerospace Center, Neustrelitz, Germany, [3]University of Colorado, Boulder, CO, USA

Abstract Advanced global navigation satellite system receivers typically report intensity scintillation indices, phase scintillation indices, and rate of total electron content change indices (ROTI). Extensive regional measurements are being accumulated and made available as diagnostic resources. Although each parameter is derived independently from measured intensity and phase time series, to the extent that ionospheric structure is the source of the scintillation manifestations, more definitive scintillation diagnostics can be predicted for structure characterized by a two-component inverse power law spectral density function. This paper derives theoretical predictions of main statistical characteristics of signal amplitude and phase that has been randomly modulated while propagating through two-dimensional random phase screens. An irregularity parameter estimation procedure is developed that generates maximum likelihood parameter estimates. It is shown that the estimated parameters reconcile theoretical prediction with reasonable accuracy. Phase-screen simulations are used to verify the theoretical predictions. The scintillation model is embedded in a generic signal model with additive noise, which allows direct application to appropriately detrended intensity and phase measurements.

Plain Language Summary Intensity, phase, and total electron content scintillation measures are collected routinely by global navigation satellite receivers and made available as diagnostic resources. This paper summarizes and demonstrates a phase-screen-model that connects the independent measures to a unified parametric model. The results provide a complete parametric characterization of the ionospheric structure that causes the scintillation.

1. Introduction

Positioning, navigation, and time synchronization (PNT) applications of global navigation satellite systems (GNSS) signals proceed from intensity, phase, and pseudo-range time series together with auxiliary information such as orbital elements. Additionally, diagnostic measurements of intensity scintillation, phase scintillation, and total electron content (TEC) structure have been made available for ionospheric phenomenology studies. To the extent that the scintillation manifestations are caused by irregularities in the earth's ionosphere, more complete diagnostic measurements can be characterized by propagation models. Vasylyev et al. (2022) have categorized models currently in use by methodology. Space weather models predict the occurrence and severity of propagation disturbances for example, Secan et al. (1995). Performance models predict system performance degradation, for example, Xu et al. (2019). Diagnostic models characterize ionospheric structure, ultimately seeking connections to the physical processes that generate the structure, for example, Rino and Carrano (2018) This paper reviews a two-dimensional phase-screen model and theoretical relations that support quantitative ionospheric structure characterization and diagnostic measurements.

The remainder of Section 1 introduces a generic intensity and phase structure model followed by a description of preprocessing operations that isolate scintillation modulation embedded in additive noise. The model excludes multi-path and interference, which can be incorporated for directed studies. Section 2 reviews two-dimensional phase-screen theory with emphasis on theoretical relations that connect observable measurements with parameterized ionospheric structure characterizations. Section 3 introduces spectral density functions, mutual coherence functions, and structure functions, which are the primary diagnostic measurements. A phase-screen model connects path-integrated phase structure to the diagnostic propagation measurements. Analytic results for a parametric two-component inverse-power-law characterization of the path-integrated phase structure are summarized. The results define expectation values of the intensity index, $S4$, the phase index, σ_ϕ, and the rate of TEC index, ROTI.

Section 3 uses phase-screen realizations to demonstrate theoretical relations that predict structure diagnostics, their intrinsic uncertainty, and the limitations imposed by noise. For example, Equation 41 predicts the noise bias of $S4$ as a function of the signal-to-noise ratio (SNR). If SNR is known or can be estimated, the $S4$ noise bias can be corrected. Moreover, GNSS processors typically incorporate coherent integration and noise cancellation to improve the SNR. We demonstrate in Section 3 that the measured SNR captures the processor enhancements. Section 4 reviews the applications of irregularity parameter estimation (IPE), which formally reconciles theoretical predictions with structure diagnostics. Scintillation degrades diagnostic structure measurements in the same way that it degrades system performance. For diagnostic measurements back-propagation removes the scintillation induced by free propagation. Our results show that IPE applied to phase structure extracted from back propagation appears to be the most efficient and robust procedure for diagnostic structure analysis. Potential limitations are discussed in Section 5.

1.1. A Generic Signal Model

For diagnostic measurements and performance evaluation, the scintillation model is embedded in a signal model that accommodates detection, demodulation, and pulse-compression operations. At the phase center of the satellite transmitting antenna the complex signal is represented as

$$v_c(t) = \sqrt{P}M(t)\exp\{2\pi i f_c t\} \tag{1}$$

where P is the transmitted power, $M(t)$ is the complex modulation, and f_c represents the carrier frequency. The signal at the phase center of a receiving antenna is a delayed replica of the transmitted signal with propagation loss and a complex modulation imparted by structure in the earth's ionosphere (The earth's atmosphere introduces an additional modulation, which is smaller and neglected in this study). Allowing for frequency translation, gains, and losses, the detected complex signal can be represented as

$$
\begin{aligned}
v_r(t) = \ & A(r(t), \mathbf{u}(t))M(t - r(t)/c)h(t; f_c)\exp\{2\pi i K \cdot TEC(t)/f_c\} \\
& \times \exp\{2\pi i f_c(t - r(t)/c)\} + \epsilon(t)/\sqrt{SNR_r},
\end{aligned}
\tag{2}
$$

where $A(r(t), \mathbf{u}(t))$ represents the signal amplitude variation as a function of range, $r(t)$, and the line-of-sight direction, $\mathbf{u}(t)$. The TEC conversion factor K is defined as

$$K = r_e c/(2\pi) \times 10^{16} = 1.345 \times 10^9 \, \text{m}^2/\text{s} \tag{3}$$

where r_e is the classical electron radius and c is the vacuum velocity of light.

Scintillation is incorporated as a frequency-dependent complex modulation, $h(t; f)$. Total electron content (TEC) is incorporated separately as a slowly varying contribution to the signal phase. Additive unity variance white noise, $\epsilon(t)$, is introduced with an a priori unknown scale factor, SNR_r, which is adjusted as described in Section 1.2 to represent the average signal to average noise power ratio.

Signal processing performed by GNSS receivers removes the modulation, establishes a phase reference, and enhances the signal intensity relative to the noise level at the point of detection. Section 3 of Kintner et al. (2007) presents a concise summary of GNSS processing. However, irrespective of the implementation details, the demodulated complex signal at the processor output, $v_d(t)$, can be represented as follows:

$$
\begin{aligned}
v_d(t) = \ & A_d(t)h(t; f_c)\exp\{2\pi i K \cdot TEC(t)/f_c + \phi_\xi(t)\} \\
& \times \exp\{2\pi i f_c t \dot{r}/c)\} + \epsilon(t)/\sqrt{SNR_d}.
\end{aligned}
\tag{4}
$$

The amplitude, $A_d(t)$, includes all gains and losses from transmission to reception. Evaluating $h(t; f)$ at $f = f_c$ assumes that the scintillation is invariant over the modulation bandwidth. The constant range rate over the demodulation processing interval, $\dot{r}$, imposes a Doppler shift, $f_c \dot{r}/c$, which the receiver must accommodate. The term $\phi_\xi(t)$ represents errors specific to signal phase extraction. The difference between SNR_r and SNR_d reflects

gains realized by detection and subsequent processing operations. Effectively, there are two unknowns in the model aside from scintillation and errors, namely $A_d(t)$ and SNR_d. Separate detrending and noise estimation operations are used to estimate the parameters as describe in the next section. From Equation 4 the sampled intensity is

$$
\begin{aligned}
I_d(n\Delta t) &= |v_d(n\Delta t)|^2 \\
&= |A_d(n\Delta t)|^2 |h(n\Delta t; f_c)|^2 + |\epsilon(n\Delta t)|^2/SNR_d \\
&\quad + 2\frac{A_d(n\Delta t)}{\sqrt{SNR_d}} \mathrm{Re}\big[h(n\Delta t; f_c)\epsilon^*(n\Delta t) \\
&\quad \times \exp\big\{\big[2\pi i K\, TEC(n\Delta t)/f_c + \phi_\xi(n\Delta t) + 2\pi i f_c n\Delta t\, \dot{r}/c\big]\big\},
\end{aligned}
\tag{5}
$$

where Δt. The sampled signal phase is

$$
\begin{aligned}
\phi_d(n\Delta t) =\ & 2\pi f_c\big(\dot{r}/c\big)n\Delta t + 2\pi K \cdot TEC(n\Delta t)/f_c + \\
& \phi_s(n\Delta t, f_c) + \phi_\xi(n\Delta t) + 2\pi M,
\end{aligned}
\tag{6}
$$

where $\phi_s(t, f_c)$ is the phase of the scintillation modulation, $h(n\Delta t; f_c)$. The $2\pi M$ ambiguity is resolved by comparing phase in wavelengths to pseudo range, which is measured and reported separately. Extracting phase from Equation 4 requires resolution of intrinsic 2π ambiguities to construct a measurement free from 2π discontinuities referred to as cycle slips.

It follows from Equation 6 that the phase at two separated, f_1 and f_2, can be combined to generate the TEC variation:

$$
\begin{aligned}
\Delta TEC(n\Delta t) =\ & \frac{\phi_d^{(2)}(n\Delta t)/f_2 - \phi_d^{(1)}(n\Delta t)/f_1}{2\pi K\big(1/f_2^2 - 1/f_1^2\big)} \\
& + \frac{\phi_s^{(2)}(n\Delta t)/f_2 - \phi_s^{(1)}(n\Delta t)/f_1}{2\pi K\big(1/f_2^2 - 1/f_1^2\big)} + \ldots
\end{aligned}
\tag{7}
$$

The omitted term in Equation 7 is the scintillation phase error, which is usually negligibly small for PNT applications, although it can be disruptive under highly disturbed conditions Breitsch et al. (2020).

1.2. Diagnostic Processing

Diagnostic processing starts with the demodulated signal Equation 4. The sampled intensity versus time represented by Equation 5 has a slow amplitude variation represented by $A_d(n\Delta t)$, a more rapid random variation caused by $h(n\Delta t; f_c)$, and an uncorrelated variation caused by noise. If the sampling is adequate to isolate the noise in the frequency domain, the noise contribution can be measured and subtracted from the signal-plus-noise intensity isolated at lower frequencies. An SNR_d estimate is obtained by subtracting the noise estimate and integrating the corrected signal contribution. The mean intensity, estimated by a curve-fitting or low-pass filtering operation, isolates the low-frequency component. Normalizing the signal to the mean intensity estimate generates a result that can be written as

$$
v_d(t) = s(t) + \epsilon(t)/\sqrt{SNR_d}.
\tag{8}
$$

The detrending operation just described imposes the constraint $\langle |v_d|^2 \rangle = 1$ over the detrending interval. The signal contribution, $s(t)$, is a narrow band process. Noting that

$$
\langle |h(t; f_c)|^2 \rangle = 1,
\tag{9}
$$

it follows that

$$s(t) = \sqrt{(1 - 1/SNR_d)}\, h(t; f_c) \exp\{2\pi i K \cdot TEC(t)/f_c + \phi_\xi(t)\}. \tag{10}$$

The angle brackets denote time averaging. It is convenient to re-normalize the detrended signal so that $\langle |v_d|^2 \rangle = SNR_d$. With either normalization the detrended signal has the form of a narrow-band locally homogeneous stochastic process, $s(t)$, in a background of additive zero-mean, unit-variance, Gaussian noise. The model supports probability-based moment estimates and error bounds Tian et al. (2020). However, realizations of the detrended signal can be processed to evaluate estimates derived from Equations 5 and 6 or $v_d(n\Delta t)$ directly without further constraining assumptions.

We assume that the time variation comes from translation of the propagation path through the structured ionosphere. If the structure is stationary over the period of measurement, an effective scan velocity, v_{eff}, converts the time variation to a projected spatial variation. The translation procedure, which depends on the scan and magnetic field directions at a central location of the structure, is described in Rino et al. (2018). The diagnostic frequency dependence, f, is measured relative to the carrier frequency f_c, which is effectively a Doppler shift. We will use the notation $f_{Dop} = f - f_c$.

2. Phase Screen Theory

2.1. Background

Scintillation theory follows from a characterization of the propagation of electromagnetic (EM) waves in structured inhomogeneous media. However, because the high mobility of charged particles along magnetic field lines, stochastic variation is confined to planes that cut across field lines Rino and Fremouw (1977). With the exception of propagation in the meridian plane, two-dimensional propagation characterizes the structure imparted to fields. The defining phase structure is formally a geometric projection of the field structure along the propagation path. The interaction of EM fields with the ionosphere is polarization dependent. However, following the development in Rino and Carrano (2021), the propagation calculation reduces to solving scalar wave equations of the form

$$\nabla^2 \psi(x,y) + k^2[1 + X(x,y)]\psi(x,y) = 0, \tag{11}$$

where $k = 2\pi f/c$, and X is the perturbation part of the square of the medium refractive index n, that is, $X = n^2 - 1$.

If $X(x,y) = 0$, the following solution to the homogeneous equation advances the field forward from x to $x + \Delta x$

$$\psi(x + \Delta x, y) = \int \hat{\psi}(x; \kappa) \exp\left\{-ik^2\sqrt{1 - (\kappa/k)^2}\, \rho_F^2\right\} \exp\{i\kappa y\} \frac{d\kappa}{2\pi}, \tag{12}$$

$$\hat{\psi}(x; \kappa) = \int \psi(x,y) \exp\{-i\kappa y\} dy, \tag{13}$$

Where κ is the spatial wavenumber in radians per meter, y is the spatial coordinate transverse to the propagation direction, and the Fresnel scale,

$$\rho_F = \sqrt{\Delta x/k}, \tag{14}$$

is introduced to facilitate the narrow-propagation-angle (paraxial) approximation. By setting $\sqrt{1 - (\kappa/k)^2} \approx 1 - (\kappa/k)^2/2$ one can approximate Equation 12 as

$$\psi(x + \Delta x, y) \simeq \exp\{-ik\Delta x\} \int \hat{\psi}(x; \kappa) \exp\left\{i(\kappa\rho_F)^2/2\right\} \exp\{i\kappa y\} \frac{d\kappa}{2\pi}. \tag{15}$$

The paraxial approximation applies when $|\kappa|/k \ll 1$. Aside from the phase factor, which translates the phase reference to the point of measurement, paraxial free propagation is characterized completely by ρ_F.

The scalar wave equation makes no distinction between vertical and horizontal complex field components, whereby $\psi(x, y)$ is formally the component of the total field projected onto the y axis. The two-dimensional wave vector

$$\mathbf{k}/k = \left[\sqrt{1 - (\kappa/k)^2}, \kappa/k\right] \tag{16}$$

defines the propagation direction of the plane-wave component with complex amplitude $\hat{\psi}(x; \kappa)$. In other words, the components of the vector Equation 16 are the cosine and sine of the propagation angle relative to the x-axis. If the field has a well defined peak, the vertical and horizontal components can be resolved. A two-dimensional medium supports horizontal fields or transverse electric fields confined to the xy plane. Surface boundary conditions are supported by uncoupled transverse and in-plane fields as reviewed in Rino and Carrano (2021).

The free propagation of the field initiated by a stochastic phase-screen is exact and can be evaluated efficiently with discrete Fourier transforms. Moreover, fields initiated by power-law processes have been studied in their own right Berry (1979). However, characterizing propagation in unrestricted inhomogeneous media is surprisingly demanding. Executing formally exact algorithms requires hours of computation for real-world problems, whereas under the paraxial approximation multiple phase-screen (MPS) calculations can be executed in minutes Knepp (1983, 2004). Phase screen equivalence replaces extended ionospheric regions with a path-integrated phase-screen located at the center of the structured region. Phase screen equivalence was demonstrated in Rino, Carrano, and Groves (2019). The remainder of this paper will review and demonstrate diagnostic applications of an equivalent two-dimensional phase-screen model.

A phase-screen realization is initiated with a realization of $\phi(y)$. As a statistically homogeneous random process $\phi(y)$ is characterized by a spectral density function (SDF), which is formally the expectation of the spatial Fourier transform intensity. A realization of the stochastic process is typically generated as

$$\phi(y) = \int \sqrt{\Phi_\phi(\kappa)} \exp\{i\kappa y\} \xi(\kappa) \frac{d\kappa}{2\pi}, \tag{17}$$

where $\Phi_\phi(\kappa)$ is the SDF and $\xi(\kappa)$ is a zero-mean unit-variance complex gaussian process with the white noise property

$$\langle \xi(\kappa)\xi^*(\kappa') \rangle = 2\pi\delta(\kappa - \kappa'). \tag{18}$$

The angle brackets denote the averaging over an ensemble of the random process realizations. The delta function is zero unless $\kappa = \kappa'$, where it is interpreted as an integrable singularity. These formal properties establish that $\langle |\hat{\phi}(\kappa)|^2 \rangle = \Phi_\phi(\kappa)$ is the SDF of $\phi(y)$. The initiating field

$$\psi_0(y) = \exp\{i\phi(y)\}, \tag{19}$$

upon transformation using Equation 13 and propagation using Equation 12 generates a phase-screen realization. To characterize the structure formally requires results from the statistical theory reviewed in the next Section. Here, we summarize critical theoretical results that depend only on the phase-screen structure as defined by the phase-screen realization and its subsequent free-space propagation.

The phase SDF, $\Phi_\phi(\kappa)$, characterizes the statistical structure that initiates observable complex fields. The defining statistical structure must be inferred from measurements of intensity and phase or the complex signal itself. Starting with the complex field, if the phase realization is a Gaussian process there is a well-known relation that connects the mutual coherence function (*MCF*) and the phase structure function (*SFN*):

$$MCF_\psi(\Delta y) = \langle \psi_0(y)\psi_0^*(y') \rangle$$
$$= \exp\{-SFN_\phi(\Delta y)/2\} \tag{20}$$

where

$$SFN_\phi(\Delta y) = \langle |\phi(y) - \phi(y')|^2 \rangle. \tag{21}$$

The SDF of a complex time series is generally referred to as a power spectral density. The term will be retained to indicate a complex field source irrespective of the time or space dependence. There is a general Fourier transform relation connecting the $MCF_\psi(\Delta y)$ and the power spectral density $PSD_\psi(\kappa)$:

$$MCF_\psi(\Delta y) = \int PSD_\psi(\kappa) \exp\{i\kappa\Delta y\} \frac{d\kappa}{2\pi}. \tag{22}$$

Because free propagation of the complex field modifies only the phase of the spatial Fourier transform, the $MCF_\psi(\Delta y)$ and $PSD_\psi(\kappa)$ are propagation invariant. The intensity and phase scintillation development is entirely the result of a structure exchange between the complex field components. This property and the associated reversibility of free propagation are well know and can be exploited.

2.2. Statistical Theory

Applying the MPS theory to a static three dimensional medium creates point samples of a two-dimensional field generated by a path integration along the direction of propagation. Formally,

$$\phi(\mathbf{r}_\perp) = -r_e c \int N_e(\mathbf{r})dx/f_c, \tag{23}$$

where $N_e(\mathbf{r})$, $\mathbf{r} = (x, y, z)$, represents the electron density in a region of interest intercepted by a path along the x direction, f_c is the carrier frequency, r_e is the classical electron radius, c is the vacuum velocity of light, and $\mathbf{r}_\perp = (y, z)$ is the spatial coordinate transverse to the propagation direction. We let

$$N_e(\mathbf{r}) = \overline{N}_e(\mathbf{r}) + \Delta N_e(\mathbf{r}), \tag{24}$$

where $\overline{N}_e(\mathbf{r})$ represents a deterministic mean and $\Delta N_e(\mathbf{r})$ represents a stochastic residual. As has been mentioned above, due to the strong anisotropy of ionospheric structure we will ignore the dependence of N_e and hence of ϕ on z. Under such convention, the reference coordinate y represents the trace of the ionospheric penetration point through the structure. It is convenient to specify the deterministic component in per kilometer TEC units as follows:

$$N_{TEC}(y) = \int \overline{N}_e(y, \boldsymbol{\eta})d\boldsymbol{\eta} \times 10^{-16} \tag{25}$$

The phase variation in radians is written as

$$\phi(y) = -2\pi K N_{TEC}(y)/f_c + \phi_s(y) \tag{26}$$

where ϕ_s represents the path integrated contribution of the stochastic ionospheric structure. The phase-screen model characterizes the stochastic ionospheric structure with an anisotropic SDF specified over a prescribed spatial wavenumber range. From the linear path-integral relation Equation 23 it can be shown that $\phi(y)$ has a complementary one-dimensional form. The relations are developed in Rino et al. (2018) and cited references.

For diagnostic applications the stochastic component of the phase-screen model is characterized by a two-component inverse power-law model defined by the four structure parameters, C_p, p_1, p_2, κ_0 as follows:

$$\Phi_\phi(\kappa) = C_p \begin{cases} \kappa^{-p_1}, \kappa \leq \kappa_0 \\ (\kappa_0^{p_2-p_1})\kappa^{-p_2}, \kappa > \kappa_0 \end{cases} \tag{27}$$

The following spectral domain relation can be constructed from the defining relation of the structure function:

$$SFN_\phi(\Delta y) = 4 \int_0^\infty [1 - \cos(\kappa\Delta y)]\Phi_\phi(\kappa)\frac{d\kappa}{2\pi} \tag{28}$$

substituting from Equation 27

$$SFN_\phi(\Delta y) = \frac{2}{\pi}C_p \int_0^{\kappa_0} \kappa^{-p_1}[1 - \cos(\kappa\Delta y)]\,d\kappa$$
$$+ \frac{2}{\pi}C_p\kappa_0^{p_2-p_1} \int_{\kappa_0}^\infty \kappa^{-p_2}[1 - \cos(\kappa\Delta y)]\,d\kappa. \tag{29}$$

The integrations can be evaluated analytically, whereby

$$SFN_\phi(\Delta y) = \frac{2}{\pi}C_p\kappa_0^{1-p_1}\left\{ \frac{1}{1-p_1}F_1 + \frac{1}{p_2-1}F_2 \right.$$
$$\left. - \frac{\pi^{3/2}}{2\cos(\pi p_2/2)}\frac{1}{\Gamma\left(\frac{p_2}{2}\right)\Gamma\left(\frac{1+p_2}{2}\right)}\left(\frac{\kappa_0\Delta y}{2}\right)^{p_2-1} \right\} \tag{30}$$

where

$$F_i = 1 - {}_1F_2\left(\frac{1-p_i}{2}; \frac{1}{2}, 1 + \frac{1-p_i}{2}; -\left(\frac{\kappa_0\Delta y}{2}\right)^2\right), \quad i = 1, 2. \tag{31}$$

and ${}_1F_2(a; b, c; x)$ is the hypergeometric function.

A complete development of the 2D phase-screen theory is presented in Carrano and Rino (2016) where it is shown that

$$\Phi_I(\mu; \rho_F, C_p, p_1, p_2, \mu_0)/\rho_F = \int_0^\infty \exp\{-\gamma(\eta, \mu)\}\exp\{-i\eta\mu\}\,d\eta, \tag{32}$$

where

$$\gamma(\eta, \mu) = \rho_F^{p_1-1}C_p 16\int_0^{\mu_0} \chi^{-p_1}\sin^2(\chi\eta/2)\sin^2(\chi\mu/2)\,d\chi/(2\pi)$$
$$+ \rho_F^{p_1-1}C_p\mu_0^{p_2-p_1}16\int_{\mu_0}^\infty \chi^{-p_2}\sin^2(\chi\eta/2)\sin^2(\chi\mu/2)\,d\chi/(2\pi). \tag{33}$$

Scale-free spatial frequency and distance variables are defined as $\mu = \kappa\rho_F$ and $\eta = y/\rho_F$, with $\mu_0 = \kappa_0\rho_F$. It was found further that intensity scintillation severity is ordered by the universal strength parameter
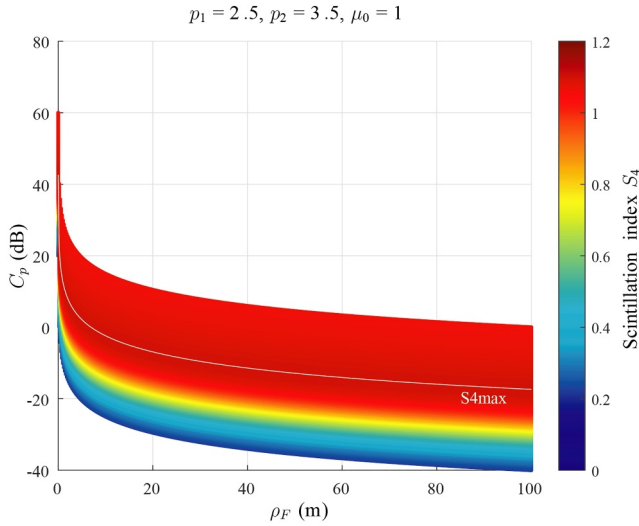
Figure 1. Display of phase-screen $S4$ versus C_p and ρ_F for structure parameters representative of low latitude scintillation. White overlaid curve is $S4$ maximum.

$$U = \rho_F^{p_1-1} C_p \begin{cases} 1, & \mu_0 \leq 1 \\ \mu_0^{p_2-p_1}, & \mu_0 > 1 \end{cases} \tag{34}$$

which is equivalent to $\Phi_\phi(\mu\rho_F)/\rho_F$ at the Fresnel frequency $\mu = 1$. Although Equations 32 and 33 comprise an analytic specification, evaluation is very demanding. A numerical integration scheme has been developed for computer evaluation. Scintillation models assume loss-free propagation, whereby $\langle I \rangle = 1$ sustained by a singularity in the intensity SDF at the origin. With this singularity removed,

$$S_4^2 = \int_0^\infty \Phi_I(\mu; \rho_F, C_p, p_1, p_2, \mu_0) \, d\mu/(\pi\rho_F) \tag{35}$$

Similarly, Equation 21 defines the phase structure function. Formally, the phase structure function defines an ROTI measure for each separation between two points of interest. However, the conditions under which the phase structure function approximates ROTI derived from TEC are impacted by scintillation. Similarly, an estimate of σ_{ϕ_s} can be derived from Equation 27

$$\sigma_{\phi_s}^2 = 2 \int_{\Delta\kappa}^{\kappa_{max}} \Phi_\phi(\kappa) d\kappa/(2\pi), \tag{36}$$

subject to similar caveats.

To summarize the scintillation range predicted by the phase-screen model with p_1, p_2, and, μ_0 fixed, Figures 1 and 2 show color displays of $S4$ as functions of C_p and ρ_F. The fixed parameters are listed in the figure titles. The overlaid white curves show the $S4$ maximum (greater than one), which identifies a region of strong focusing. As ρ_F increases $S4$ converges to a saturation value, which can be larger than one. From multi-frequency $S4$ measurements alone it would be difficult to distinguish different power-law structure. Defining structure parameter estimation will be described in Section 4.

3. Diagnostic Measurements

The theoretical relations up to this point related theoretical expectation calculations of spectral density functions and periodogram measurements. Diagnostic measurements are interpreted as being applied to sampled realizations of random processes. The simplest diagnostic measurements are sample moments of m-th order as

$$M_m(I) = \frac{1}{N} \sum_{n=1}^{N} I^m(n\Delta t). \tag{37}$$

Where $I(n\Delta t)$ is a sample of a stochastic process, which includes noise. The number of samples used reduces the intrinsic uncertainty and the uncertainty due to additive noise. The number of samples, N, is limited by statistical uniformity, meaning realizations with the same number of samples produce the same expectation result. Because moments grow rapidly as the order increases, fractional moments,
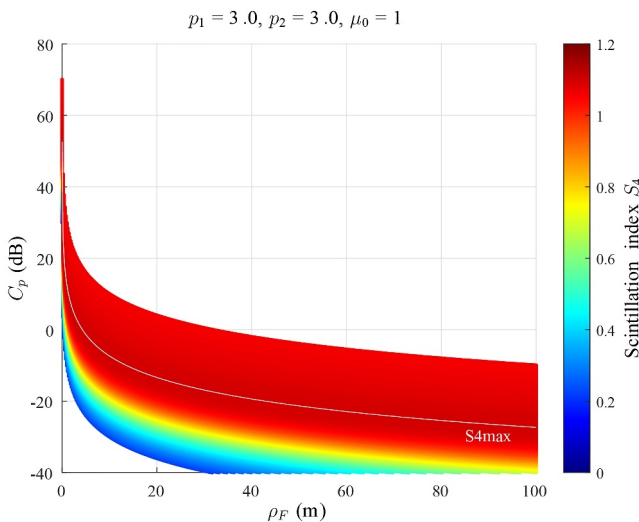
$$M_m(I)/M_1(I)^m, \tag{38}$$

Figure 2. Display of phase-screen $S4$ versus C_p and ρ_F for single power-law structure parameters typically used for scintillation models. White overlaid curve is $S4$ maximum.
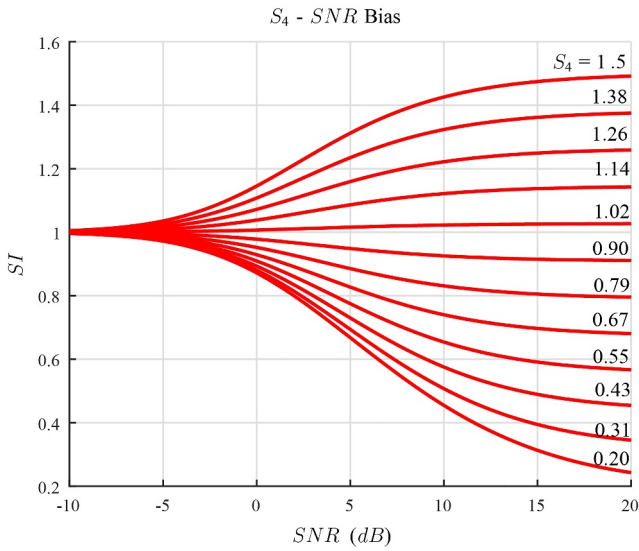
are preferred for diagnostic analysis. The measured scintillation index is defined as

Figure 3. Display of *SI* versus *SNR* showing transition from noise domination (*SNR* < 0 dB) to signal domination (*SNR* > 20 dB).

$$\widehat{S4} = \sqrt{M_2(I)/M_1(I)^2 - 1}. \tag{39}$$

Expectation follows from a statistical model. For example, if the intensity has an exponential distribution

$$\langle M_m(I)\rangle / \langle M_1(I)^m\rangle = m!, \tag{40}$$

whereby $\langle \widehat{S4} \rangle = 1$.

Additive noise affects and ultimately dominates moment measurements. In Appendix A we show that the measured noise bias of the measured scintillation index, denoted *SI*, can be calculate if the *SNR* is known as follows:

$$SI^2 = \frac{S4^2 + 2/SNR + 1/SNR^2}{1 + 2/SNR + 1/SNR^2}, \tag{41}$$

where *SI* is the expectation of the scintillation index derived from a signal embedded in additive uncorrelated noise.

Figure 3, which is constructed using Equation 41, shows the expected transition from noise domination where $SI \sim 1$ to high *SNR* (>20 dB) where $SI \sim S4$. If *SNR* is known, measured *SI* estimates can be corrected by inverting Equation 41, subject to uncertainty in the measurement of *SI* and *SNR*.

In the introduction we argued that the generic signal model represented by Equation 4 captures the effects of the processing details shown, for example, in Figure 14.17 in Morton et al. (2011). The carrier-to-noise-ratio (C/N0) introduced in Chapter 6.7 of J. Spilker (1977) is a processor-specific figure of merit that accommodates processing gain. However, extrapolating or simulating processor performance requires explicit knowledge of effective noise level. The relation between SNR_d and C/N0 is described in detail Sharawi et al. (2007). Formally,

$$C/N0 = SNR_d\, BW, \tag{42}$$

where BW is a waveform-dependent bandwidth measure with frequency units. Equations 7 and 8 in Sharawi et al. (2007), when written in complex form with additive noise are functionally identical to Equation 4. The power ratio method described in this reference contains an *SNR* estimation procedure identical to the procedure described our Section 2.

To demonstrate model applications for interpreting processor-independent diagnostic measurements we focus our attention on the signals from Global Positioning System (GPS). To this end, the generic L1, L2, and L5 GPS simulations were generated at one kHz for one-hour periods. To simulate multi-frequency signals passing through identical structure one reference phase realization is used. Subsequent realizations are generated with the extrapolated frequency-dependent U, μ_0, and ρ_F parameters. The sample rate is representative of Equation 4 at the correlator output prior to coherent noise suppression. To provide a range of propagation disturbance levels, the phase-screen U parameter was varied for each one-minute segment. The segment sampling is sufficient to accommodate varying N values or coherent noise suppression with representative M sampling. The left frames in Figure 4 show, respectively, the L1, L2, and L5 realizations. The 10 dB SNR is a low value for an operational system. The red circles in the right frames are the true $S4$ values for each segment. Intensity moments were estimated over 15 s intervals and averaged. The blue curves in the right frames are the *SI* estimates derived from the signal moments at 4 estimates per minute. The variation is dominated by the intrinsic random-process uncertainty. However, *SI* estimates are also biased by the noise contribution. The green lines in the left frames are estimates of the SNR derived from the intensity spectrum over the segment interval. The green points in the right frames are corrected *SI* estimates derived by inverting Equation 41. Within the intrinsic measurement uncertainty the bias is completely removed, which verifies Equation 41 and its utility for scintillation bias correction.
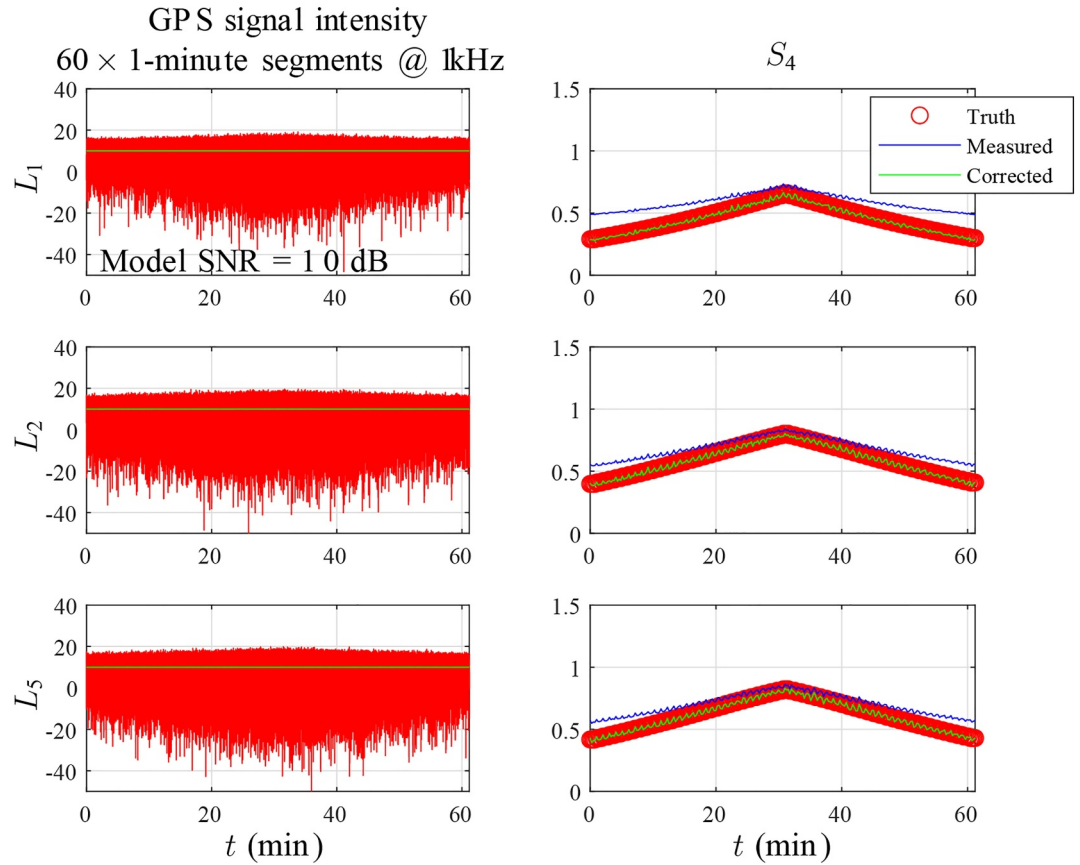
Figure 4. Left frames show intensity realizations at 1-kHz with the average SNR (10 dB) overlaid. The right frames show, as indicated, the true *S*4 (red), measured SI over 15-s intervals (blue), and the corrected SI (green).

The *S*4 noise bias estimates shown in Figure 4 are significantly larger than noise biases observed with data from commercial GPS processors. The *S*4 noise bias is rarely significant. In the early development of GPS processors Van Dierendonck et al. (1993) proposed an intensity estimate derived from the difference between coherent (narrow band, NBP) and incoherent (wideband, WBP) intensity averages. Formally

$$ID = NBP - WBP \tag{43}$$

where

$$WBP = \sum_{0}^{M} |v_m|^2 \tag{44}$$

$$NBP = \left| \sum_{0}^{M} v_m \right|^2 \tag{45}$$

An estimate of the *S*4 noise bias similar to Equation 41 was derived using the GPS-specific *C/N*0 measure. The Van Direndonck correction was demonstrated in Zhang et al. (2010).

To simulate the Van Direndonck scheme, representative *ID* realizations were generated with $M = 20$, which produces intensity samples at 50 Hz, a commonly reported sample rate for high-end diagnostic GPS receivers. The left frames in Figure 5 show the IS intensity with the measured L1 SNR_d indicated. The blue points in the right frames are *SI* estimates derived over full segment intervals. The results are in good agreement with the true *S*4 values. The measured SNR_d values indicate more than 8 dB of processing gain is realized with the Van
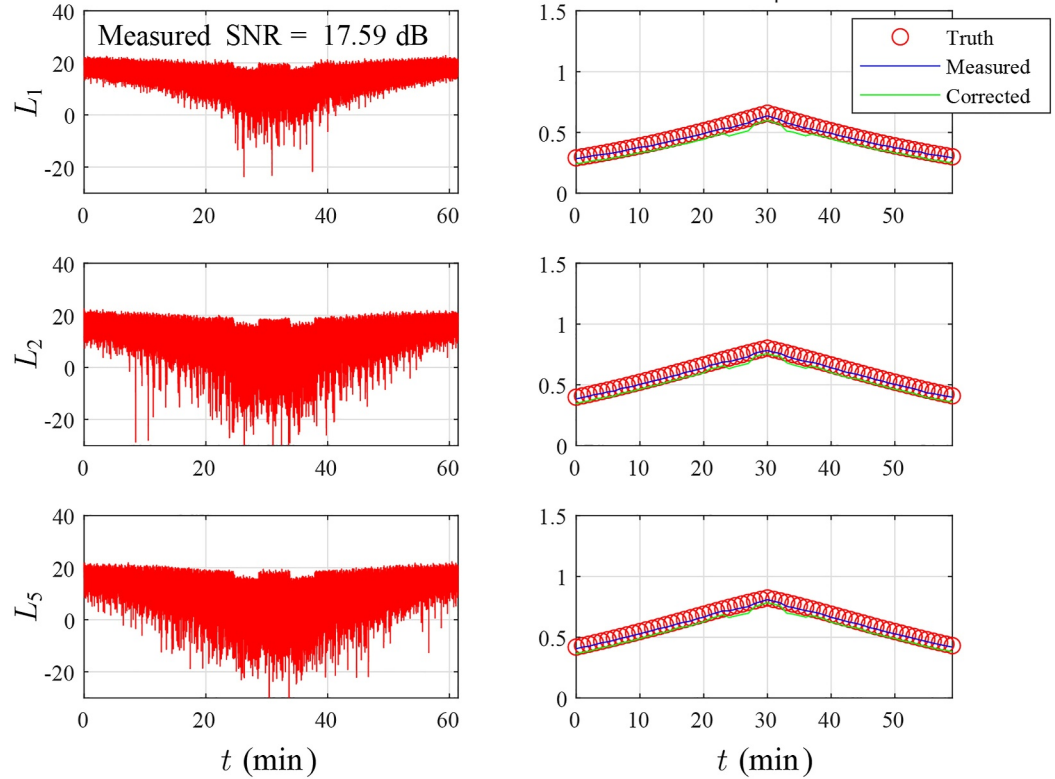
Figure 5. The left frames show IS at 50 Hz ($M = 20$). The right frames show, as indicated, the true $S4$, measured SI over 1-min intervals, and the corrected SI.

Dierendonk scheme. The bias correction at the higher SNR_d level is small, which is consistent with the analysis reported by Zhang et al. (2010). Using the measured SNR_d in Equation 41 will correct the noise bias irrespective of coherent noise cancellation. However, we note that independent of the noise bias the level changes between 20 and 40 min indicate sensitivity of the Van Direndonck scheme to discontinuous intensity changes.

3.1. Structure Parameter Estimation

Parameter estimation starts with establishing a parameterized structure model. Phase screen realizations are defined by five structure parameters, namely C_p, p_1, κ_0, p_2 and the Fresnel scale ρ_F. The phase-screen statistical theory summarized in Section 2.2 connects the parameterized structure model to diagnostic structure measures. Irregularity parameter estimation is a maximum likelihood estimation procedure that reconciles statistical theory predictions with diagnostic measurements. The left frames in Figure 6 show L1, L2, and L5 realizations presented in spatial units, which relate more directly to the structure characteristics. The structure parameters are representative of developed equatorial scintillation. The red curves in the right frame show the initiating phase $\phi(y)$, cf. Equation 26, for each realization. The blue curves show the phase reconstructed from the complex signal. Because model realization phase is a derived quantity, there is no phase truth as such. Sampling can affect the reconstruction Rino et al. (2020).

The left frames in Figure 7 show the measured realization intensity SDFs (red) with the theoretical predictions overlaid (green). The right frames in 7 show the measured complex realization PSDs (red) with the theoretical predictions overlaid. Although the results are not shown because of the very good agreement between the measured diagnostics (red), and the theoretical predictions (green) IPE recovers the parameters used to generate the realizations. As discussed in Rino and Carrano (2018) the minimization procedure exploits the known limiting statistics of periodograms to form maximum-likelihood estimates. The effectiveness of IPE applied to measured diagnostics depends on the complexity of the theoretical models and the number of parameters being estimated as well as measurement errors and noise. The most demanding is IPE applied to the intensity SDF
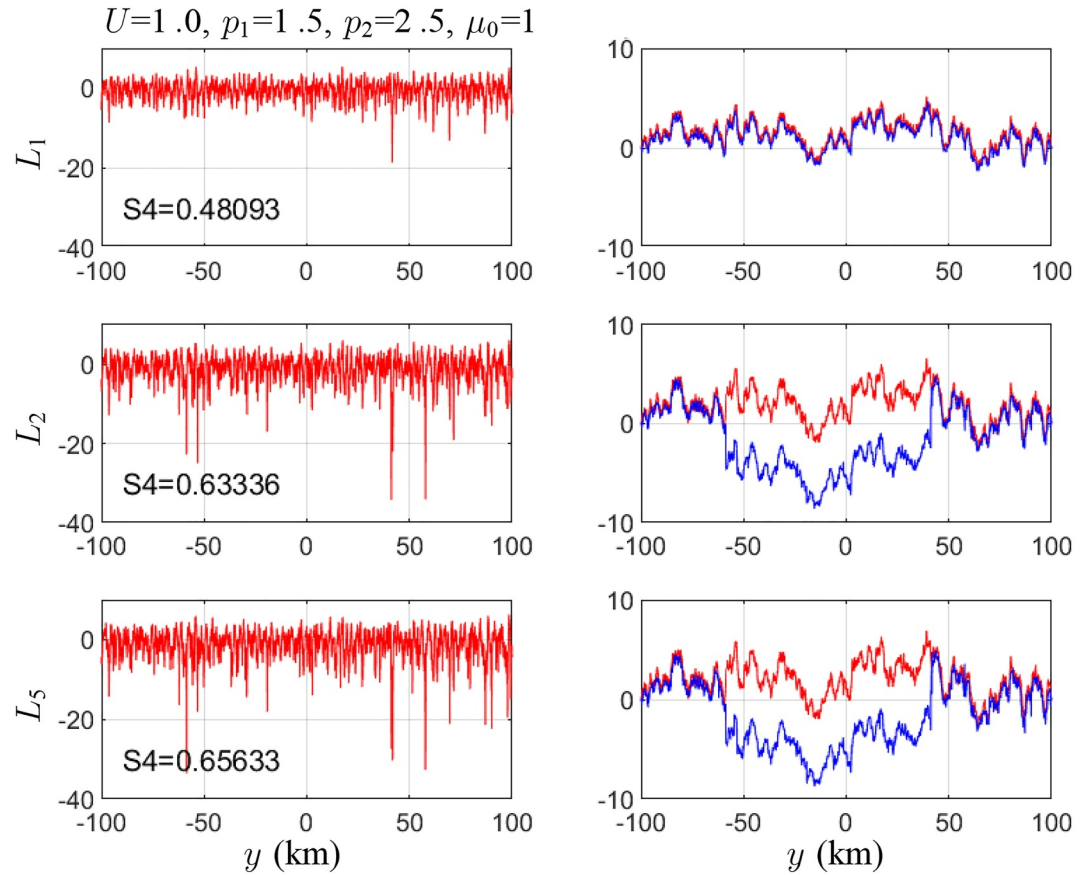
Figure 6. Left frames show Global Positioning System phase-screen simulations for L1, L2, and L5 frequencies. The reported scintillation index is measured. Right frames show the initiating phase (red) and the reconstructed phase from the complex scintillation (blue).

$\Phi_I(\mu; \rho_F, C_p, p_1, p_2, \mu_0)/\rho_F$ as defined by Equations 32 and 33, which has been used effectively by Carrano et al. (2017) and Xu et al. (2019). However, the computational and procedural details are too demanding for routine applications.

Insofar as we know, no attempts have been made to apply IPE to measured PSDs, nor to structure functions derived from MCF estimates, which are theoretically connected by Equation 21. However, Carrano et al. (2019) exploited the *ROTI* MCF relation under weak scatter conditions to demonstrate and exploit an *ROTI* *S*4 relation. Similarly, under weak-scatter conditions *TEC* structure can be interpreted as a direct measure of path-integrated irregularity structure Rino, Morton, et al. (2019).

To demonstrate PSD, SDF, and SFN relations, Figure 8 shows the simulated L1 PSD from Figure 7 (blue) with the theoretical PSD overlaid (red). The middle frame shows the MCF, which is the inverse Fourier transform of the PSD. The lower frame shows the structure function derived from the relation $SFN = -2\log(MCF)$ with the analytic form Equation 30 overlaid. The computation of the MCF using the analytic relation $MCF = \exp(-SFN/2)$ is also overlaid. The structure function at each separation can be identified with a corresponding ROTI measure upon conversion to time separation. Alternatively, the complete SFN could be used as a diagnostic measure. An unconstrained power-law SDF is singular at the zero frequency limit, although the structure function is well defined for a range of power-law index values. The asymptotic behavior of the structure function as the separation approaches zero is used to define a structure constant in turbulence theory. This is illustrated in the lower frame in 8. The overlaid green curve is a power-law fit. The complementary power-law behavior between the *SDF* and the structure function is well know in turbulence theory.
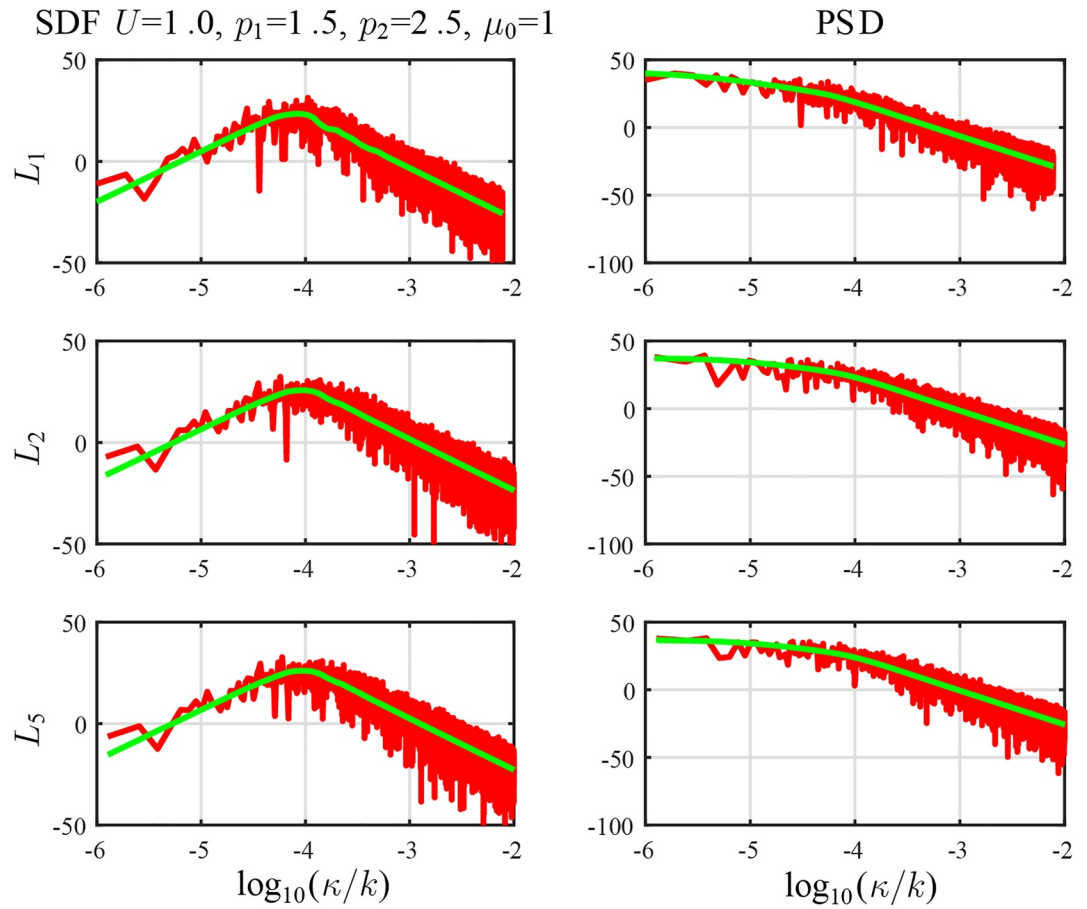
Figure 7. Left frames show measured (red) and predicted intensity SDFs (green). Right frames show measured (red) and predicted complex signal PSDs (green).

3.2. Back Propagation

A direct estimate of the defining phase structure can be obtained by exploiting the fact that free-propagation is reversible. From the two-dimensional theory a measured field admits the exact representation

$$\psi(x, y = t\, v_{eff}) = \int \hat{\psi}(x; \kappa) \exp\left\{-ik^2 \sqrt{1 - (\kappa/k)^2}\, \rho_F^2\right\}$$
$$\times \exp\{i\kappa\, t\, v_{eff}\} d\kappa/(2\pi). \tag{46}$$

The intensity of a back-propagated field generates a well-defined minimum of intensity variation (quantified by e.g. S_4) that can be determined efficiently with standard minimization algorithms. The spatial domain propagator has been converted to time-domain units for time-series applications. The scaled propagation distance is a parameter that can be converted to true distance from the known propagation geometry. Evaluating the propagation integral at an arbitrary distance generates a starting intensity.

Figure 9 shows the result of applying back propagation to the simulation summarized in Figure 6. The green curves overlaid in the left frames show back-propagated intensity, which is very near one (or zero dB). The blue curves in the right frames show the reconstructed phase from the back propagated field. In the absence of intensity variation phase unwrapping generally produces no phase jumps. This is illustrated in Figure 9, which shows that the initiating phase $\phi(y)$ is recovered. Breitsch and Morton Breitsch and Morton (2023) exploited this property to correct measured phase jumps. The back propagation concept is described in Wagen and Yeh (1985). Applications for one- and two-way propagation are described in Carrano et al. (2012). For occultation geometries back propagation is used to estimate a central location of the structure along an extended path Ludwig-Barbosa
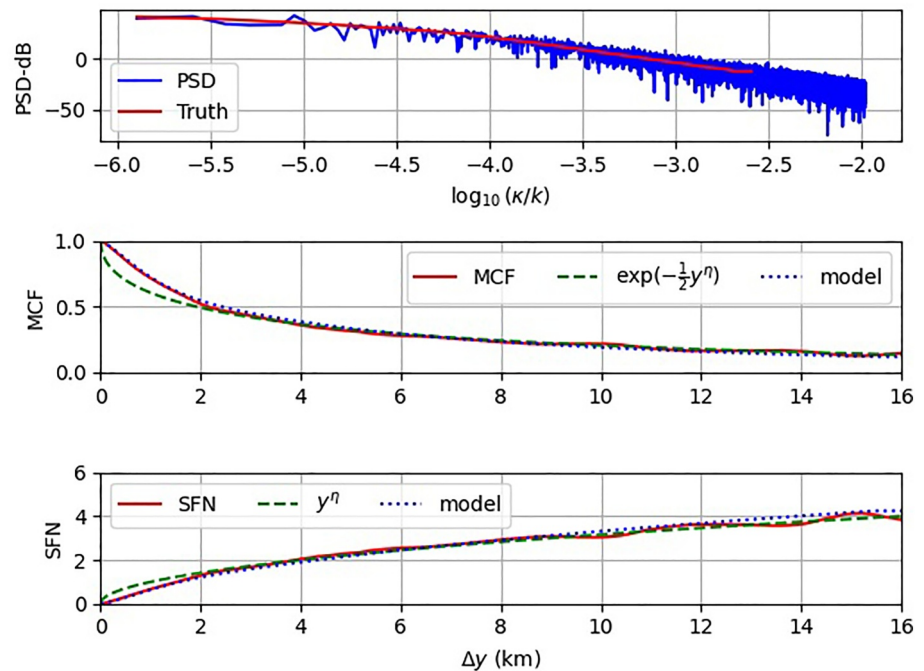
Figure 8. The top frame is a repeat from Figure 7, right panel, of the measured PSD (blue) and the theoretical result for L_1 signal. The middle frame shows the defining portion of the MCF. The lower frame is the derived structure function (red) with a power-law fit (green). The red solid lines in the middle and lower frames represent the theoretical MCF and SFN functions. The green dashed lines represent a power-law fit with $\eta = 0.5$. The blue dotted lines are obtained from Equation 30.

et al. (2023). Limitations imposed by fields that are not highly anisotropic and noise are discussed in the cited references. Insofar as we know, there has been no attempt to recover the equivalent phase for structure analysis.

4. Summary and Conclusions

We have reviewed a two-dimensional phase-screen model embedded in a generic signal model. The model applications include simulations for processor performance evaluation and interpreting diagnostic measurements. The defining relations represented by Equations 4–7 are applicable to any digitally reported satellite signals after demodulation. Detrending and *SNR* estimation translate the data for direct comparisons with phase-screen simulations or interpretation using theoretical predictions. Path-integrated structure is characterized with a two-component inverse power-law model Equation 27. The objective of diagnostic measurements is to estimate the defining structure parameters and the propagation distance. IPE as summarized in Section 4 can be applied to estimate parameters that reconcile theoretical predictions with measurements.

Our objective was to demonstrate unifying quantitative diagnostic structure measurements with simulations that include additive noise and *SNR* improvements commonly realized by post-detection coherent processing as well as resolution sensitivity trades. Whereas, first-order scintillation diagnostics are routinely used for morphological studies, few attempts have been made to identify systematic structure changes that might otherwise be overlooked. It is also important to recognize that the defining phase-screen structure is an abstract measure unique to the equivalent phase screen model. Validation of the procedures requires demonstrated consistency with real data, which is the planned next phase of development.

In this regard we have suggested the use of back propagation for improving structure diagnostics. Back propagation was introduced as a means of removing diffraction and thereby isolating the defining phase structure. In Section 3.2 we verified that back propagation will perfectly recover the defining SDF with no prior knowledge of the propagation distance. Back propagation has been used extensively, but mainly to localize propagation disturbances in occultation measurements. Limitations are imposed by the largest intervals that generate measurable intensity structure. In effect, diffraction-free TEC structure is the upper limit of back propagation and a working definition of the intermediate scale upper limit.
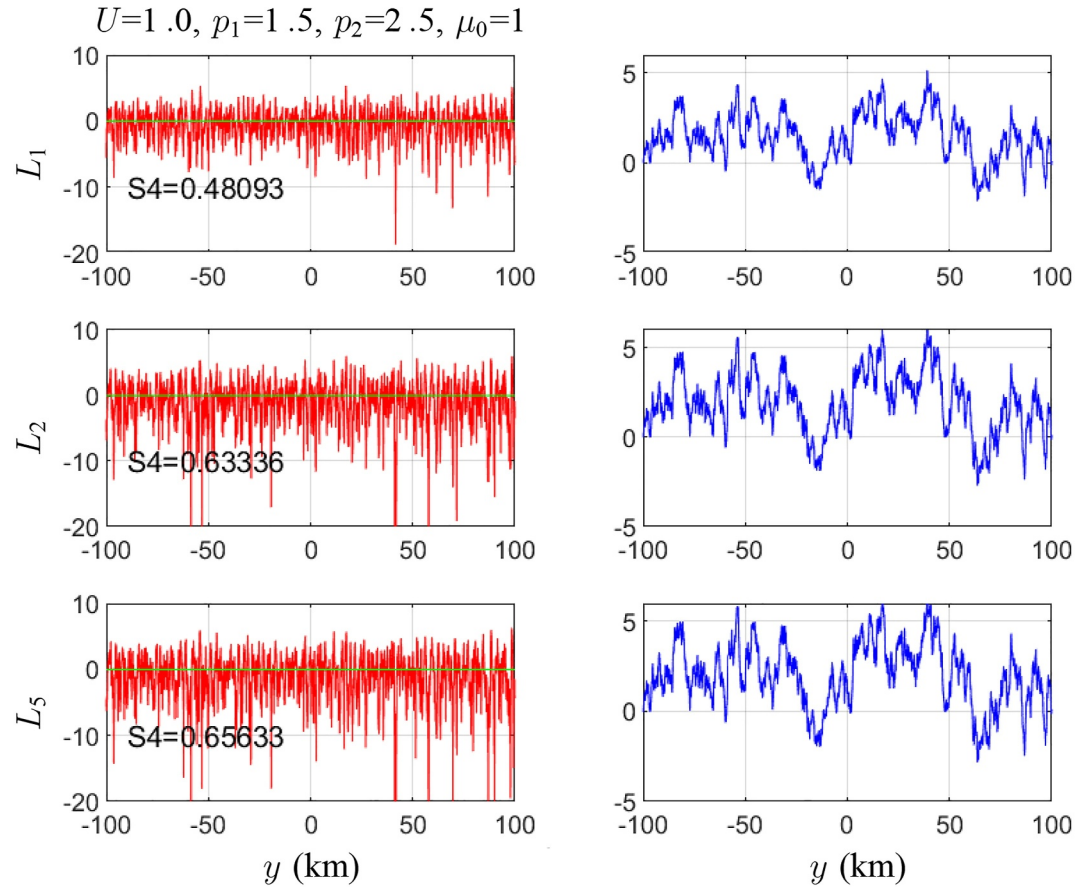
Figure 9. Left frames repeat Global Positioning System intensities from realizations shown in left panels of Figure 6. Green overlaid curves show back propagated field intensities. Right frames show initiating phase (red, covered by the blue curve) with phase derived from back propagated signals (blue). Plotted differences are imperceptible.

The issues include detrending and data segmentation, which identifies homogeneous segments that are amenable to statistical measurement. Phase is particularly challenging because it must be reconstructed from a complex signal dominated by large-scale range change and imposed TEC structure. No phase structure diagnostics have been introduced largely because there is no theory that predicts phase structure under highly disturbed conditions. However, to the extent that simulations accurately predict the complex fields, analysis procedures can be evaluated. This is the general approach taken to evaluate TEC measurement accuracy Breitsch et al. (2020).

Appendix A

A1. S4 Bias Correction

From Equation 8 the signal model consists of two additive uncorrelated stochastic processes. If we assume further that the underlying stochastic processes are homogeneous, the moments defined by Equation 37 can be computed directly as follows.

$$v = s + n \tag{A1}$$

$$I = |v|^2 \tag{A2}$$

$$\langle I^2 \rangle = \langle |s|^4 \rangle + 4\langle |s|^2 \rangle \langle |n|^2 \rangle + \langle |n|^4 \rangle \tag{A3}$$

$$\langle I \rangle^2 = \langle |s|^2 \rangle^2 + 2\langle |s|^2 \rangle \langle |n|^2 \rangle + \langle |n|^2 \rangle^2, \tag{A4}$$

It follows that the intensity variance can be written as

$$\left(\langle I^2\rangle - \langle I\rangle^2\right) = \left(\langle |s|^4\rangle - \langle |s|^2\rangle^2\right) + 2\langle |s|^2\rangle\langle |n|^2\rangle + \langle |n|^4\rangle - \langle |n|^2\rangle^2. \tag{A5}$$

If the noise intensity, n^2, is exponentially distributed, then:

$$\langle n^4\rangle - \langle n^2\rangle^2 = \langle n^2\rangle^2. \tag{A6}$$

The result simplifies to:

$$\langle I^2\rangle - \langle I\rangle^2 = S_4^2\langle s^2\rangle^2 + 2\langle s^2\rangle\langle n^2\rangle + \langle n^2\rangle^2. \tag{A7}$$

Normalizing to the average noise intensity replaces the average signal intensity with one and the average noise intensity with $1/SNR$, whereby.

$$\langle I^2\rangle - \langle I\rangle^2 = S_4^2 + 2/SNR + 1/SNR^2 \tag{A8}$$

$$\langle I\rangle^2 = 1 + 2/SNR + 1/SNR^2 \tag{A9}$$

Forming the ratio leads to the desired result:

$$SI = \left(S_4^2 + 2/SNR + 1/SNR^2\right)^{1/2}/\left(1 + 2/SNR + 1/SNR^2\right)^{1/2}. \tag{A10}$$

Data Availability Statement

No data were used in the paper. All the results can be reconstructed as described in the paper.

References

Berry, M. V. (1979). Diffractals. *Journal of Physics A: Mathematical and General*, *12*(6), 781–797. https://doi.org/10.1088/0305-4470/12/6/008

Breitsch, B., & Morton, Y. T. (2023). Mitigation of global navigation satellite system cycle slips due to scintillation using radio backpropagation. *Institute of Navigation*, *70*(3), 593. https://doi.org/10.33012/navi.593

Breitsch, B., Morton, Y. T., Rino, C., & Xu, D. (2020). GNSS carrier phase cycle slips due to diffractive ionosphere scintillation: Simulation and characterization. *IEEE Transactions on Aerospace and Electronic Systems*, *56*(5), 3632–3644. https://doi.org/10.1109/TAES.2020.2979025

Carrano, C. S., Groves, K. M., & Caton, R. G. (2012). The effect of phase scintillations on the accuracy of phase screen simulation using deterministic screens derived from GPS and ALTAIR measurements. *Radio Science*, *47*(4), RS0L25. https://doi.org/10.1029/2011RS004958

Carrano, C., & Rino, C. (2016). A theory of scintillation for two-component power law irregularity spectra: Overview and numerical results. *Radio Science*, *51*(6), 789–813. https://doi.org/10.1002/2015RS005903

Carrano, C. S., Groves, K. M., & Rino, C. L. (2019). On the relationship between the rate of change of total electron content index (ROTI), irregularity strength (CkL) and the scintillation index (S4). *Journal of Geophysical Research: Space Physics*, *124*(3), 2099–2112. https://doi.org/10.1029/2018JA026353

Carrano, C. S., Rino, C. L., & Groves, K. M. (2017). Maximum likelihood estimation of phase screen parameters from ionospheric scintillation spectra. In *15th international ionospheric effects symposium* (pp. 1–11).

Kintner, P. M., Ledvina, B. M., & de Paula, E. R. (2007). GPS and ionospheric scintillations. *Space Weather*, *5*(9), S09003. https://doi.org/10.1029/2006SW000260

Knepp, D. L. (1983). Multiple phase-screen calculation of the temporal behavior of stochastic waves. *Radio Science*, *71*(6), 722–737. https://doi.org/10.1109/PROC.1983.12660

Knepp, D. L. (2004). Effects of ionospheric scintillation on Transit satellite measurement of total electron content. *Radio Science*, *39*(1), RS1S11. https://doi.org/10.1029/2002RS002825

Ludwig-Barbosa, V., Rasch, J., Sievert, T., Carlström, A., Pettersson, M. I., Vu, V. T., & Christensen, J. (2023). Detection and localization of F-layer ionospheric irregularities with the back-propagation method along the radio occultation ray path. *Atmospheric Measurement Techniques*, *16*(7), 1849–1864. https://doi.org/10.5194/amt-16-1849-2023

Morton, Y. J., Van Dioggelen, F., Spilker, J. J. J., & Parkinson, B. W. (2011). *Position, navigation and timing technologies in the 21st century*. Wiley.

Rino, C., Breitsch, B., Morton, Y., Xu, D., & Carrano, C. (2020). GNSS signal phase, TEC, and phase unwrapping errors. *Navigation*, *67*(4), 865–873. https://doi.org/10.1002/navi.396

Rino, C., & Carrano, C. (2018). On the characterization of intermediate-scale ionospheric structure. *Radio Science*, *53*(11), 1316–1327. https://doi.org/10.1029/2018RS006709

Rino, C., & Carrano, C. (2021). A vector theory for forward propagation in a structured ionosphere. *Journal of Atmospheric and Terrestrial Physics*, *215*, 105558. https://doi.org/10.1016/j.jastp.2021.105558

Rino, C., Carrano, C., & Groves, K. (2019). Wave propagation in extended highly anisotropic media. *Radio Science*, *54*(7), 646–659. https://doi.org/10.1029/2019RS006793

Rino, C., & Fremouw, E. (1977). The angle dependence of singly scattered wavefields. *Journal of Atmospheric and Terrestrial Physics*, *39*(8), 859–868. https://doi.org/10.1016/0021-9169(77)90166-0

Rino, C., Morton, Y., Brietsch, B., & Carrano, C. (2019). Stochastic TEC structure characterization. *JGR Space Physics*, *124*(12), 10571–10579. https://doi.org/10.1029/2019JA026958

Rino, C., Yokoyama, T., & Carrano, C. (2018). Dynamic spectral characteristics of high-resolution simulated equatorial plasma bubbles. *Progress in Earth and Planetary Science*, *5*(1), 83. https://doi.org/10.1186/s40645-018-0243-0

Secan, J. A., Bussey, R. M., Fremouw, E. J., & Basu, S. (1995). An improved model of equatorial scintillation. *Radio Science*, *30*(3), 607–617. https://doi.org/10.1029/94RS03172

Sharawi, M. S., Akos, D. M., & Aloi, D. N. (2007). GPS C/N0 estimation in the presence of interference and limited quantization levels. *IEEE Transactions on Aerospace and Electronic Systems*, *43*(1), 227–238. https://doi.org/10.1109/TAES.2007.357129

Spilker, J. (1977). *Digital communications by satellite*. Prentice Hall.

Tian, Y., Wang, X., Sun, Y., Du, Q., Bai, W., Cai, Y., et al. (2020). Error analysis on ionospheric scintillation index S4 measured by GNSS receiver. *GPS Solutions*, *24*(75), 1–13. https://doi.org/10.1007/s10291-020-00987-y

Van Dierendonck, A. J., Klobuchar, J., & Hua, Q. (1993). Ionospheric scintillation monitoring using commercial single frequency C/A code receivers. In *Proc. ION ITM* (pp. 1333–1342).

Vasylyev, D., Béniguel, Y., Wilken, V., Kriegel, M., & Berdermann, J. (2022). Modeling of ionospheric scintillation. *J. Space Weather Space Clim.*, *12*(22), 22. https://doi.org/10.1051/swsc/2022016

Wagen, J. F., & Yeh, K. C. (1985). Simulation of HF propagation and angle of arrival in a turbulent ionosphere. *Radio Science*, *24*(2), 196–208. https://doi.org/10.1029/RS024i002p00196

Xu, D., Morton, Y., & Yang, R. (2019). A comparative performance analysis of advanced gnss carrier tracking algorithms during strong equatorial ionospheric scintillation. *IEEE Transactions on Aerospace and Electronic Systems*.

Zhang, L., Morton, Y., van Graas, F., & Beach, T. (2010). Characterization of GNSS signal parameters under ionosphere scintillation conditions using software-based tracking algorithms. In *IEEE/ION position location and navigation symposium* (pp. 264–275). https://doi.org/10.1109/PLANS.2010.5507209